

Supplementary Materials for

Nanoparticle elasticity regulates phagocytosis and cancer cell uptake

Yue Hui, Xin Yi, David Wibowo, Guangze Yang, Anton P. J. Middelberg, Huajian Gao*, Chun-Xia Zhao*

*Corresponding author. Email: huajian.gao@ntu.edu.sg (H.G.); z.chunxia@uq.edu.au (C.-X.Z.)

Published 17 April 2020, *Sci. Adv.* **6**, eaaz4316 (2020)
DOI: 10.1126/sciadv.aaz4316

The PDF file includes:

Figs. S1 to S9
Table S1
References

Other Supplementary Material for this manuscript includes the following:

(available at advances.sciencemag.org/cgi/content/full/6/16/eaaz4316/DC1)

Movies S1 and S2

Supplementary characterization of SNCs

1). DLS results of unmodified and PEG-modified SNCs

(a) Size, PDI and ζ potential of unmodified SNCs (values are means, n = 3).

| Molar percentage of TEOS | 0 | 5 | 10 | 20 | 40 | 100 |
|--------------------------|-------|-------|-------|-------|-------|-------|
| Z-averaged diameter [nm] | 185 | 185 | 186 | 186 | 189 | 196 |
| PDI | 0.11 | 0.13 | 0.14 | 0.08 | 0.13 | 0.09 |
| ζ potential [mV] | +29.0 | +29.2 | +27.3 | +30.5 | +30.0 | +28.0 |

(b) Size, PDI and ζ potential of the softest and stiffest, PEG-modified SNCs (values are means, n = 3).

| Molar percentage of TEOS | 0 | 100 |
|--------------------------|------|------|
| Z-averaged diameter [nm] | 202 | 211 |
| PDI | 0.06 | 0.03 |
| ζ potential [mV] | -1.7 | -1.7 |

Fig. S1. DLS results of (a) unmodified and (b) PEG-modified SNCs.

2). Supplementary TEM micrographs for SNCs

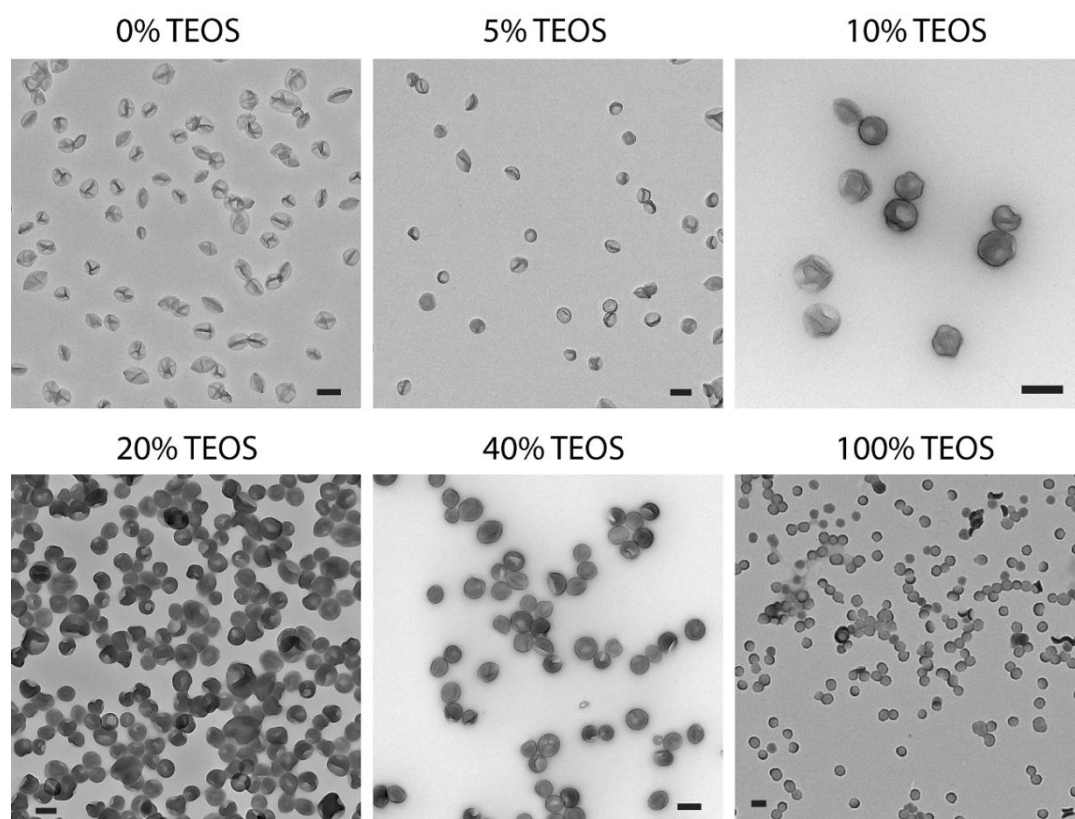


Fig. S2. TEM images of SNCs made by TEVS/TEOS mixtures with different molar percentage of TEOS. Scale bars = 200 nm.

3). Measurement of SNC mechanical property using AFM

The mechanical properties of SNCs were measured in using the force mapping technique of liquid phase AFM. Force-indentation curves of SNCs were obtained and fitted using Hertzian contact model to calculation their Young's moduli. The purple and black colored areas in the Young's modulus maps represent the false fitting results of the mica substrates as force-indentation curves had very high gradient (Fig. S3b).

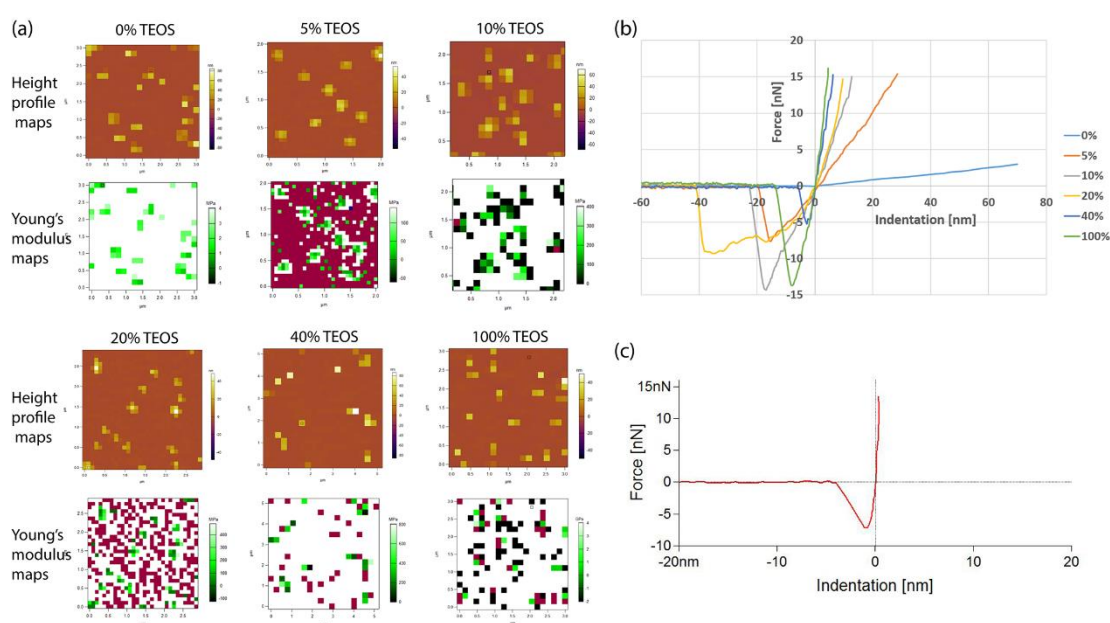


Fig. S3. (a) AFM height profile maps and Young's modulus maps of the SNCs. Purple and black colored areas represent false fitting results of the mica substrates. (b) Representative force-indentation curves of SNCs prepared using TEVS/TEOS mixtures having different percentages of TEOS. (c) A representative force-indentation curve of mica substrate.

Quantification of PEG density on the surfaces of SNCs

1). Experimental method for PEG density quantification

The PEG density on the surface of modified SNCs was quantified using a spectrophotometric method reported previously (Fig. S4a) (41), in which the conjugation density of mPEG-NHS on protein nanocages was measured using fluorescence density by replacing mPEG-NHS with fluorescently labelled FITC-PEG-NHS. Following this method, in the current work, prepared SNCs were surface-modified with 7.2 mM of mPEG-NHS and 0.8 mM of FITC-PEG-NHS for 16 h at 4 °C in HEPES buffer (25 mM, pH 7.5). After surface modification, the particle concentrations of SNCs were determined by NanoSight and the SNCs were centrifuged (21885 ×g, 20 min) and washed twice and collected by centrifuge (21885 ×g, 20 min). The SNC pellet was then dissolved in Tris-base buffer (1 mM, pH 10) to decompose the SNCs. The obtained solution containing FITC-PEG was then diluted by a factor of 10, with its fluorescence intensity measured using a microplate reader (Infinite M200 PRO, Tecan, Männedorf, Switzerland). The fluorescence intensity was then used to determine the concentration of FITC-PEG using a fluorescence intensity–concentration standard curve of FITC-PEG in the Tris-base buffer (1M, pH 10) (Fig. S4b). Fig. S4c displays the fluorescence intensity change of 50 and 500 nM of FITC-PEG-NHS solution in HEPES buffer (25 mM, pH 7.5) at 4 °C (which is the condition of the PEGylation reaction) over 24 h, with no obvious fluorescence change observed, meaning that the fluorescence intensity of FITC-PEG did not change significantly during the 16 h PEGylation.

2). NanoSight technique for quantifying the particle concentrations of SNCs

The particle concentrations of SNCs were determined by nanoparticle tracking analysis (NTA) using a Malvern NanoSight NS300 (ATA Scientific PTY LTD, Taren Point, Australia). The SNCs were diluted to a concentration range of 50 to 150 particles per frame to ensure the accurate measurement.

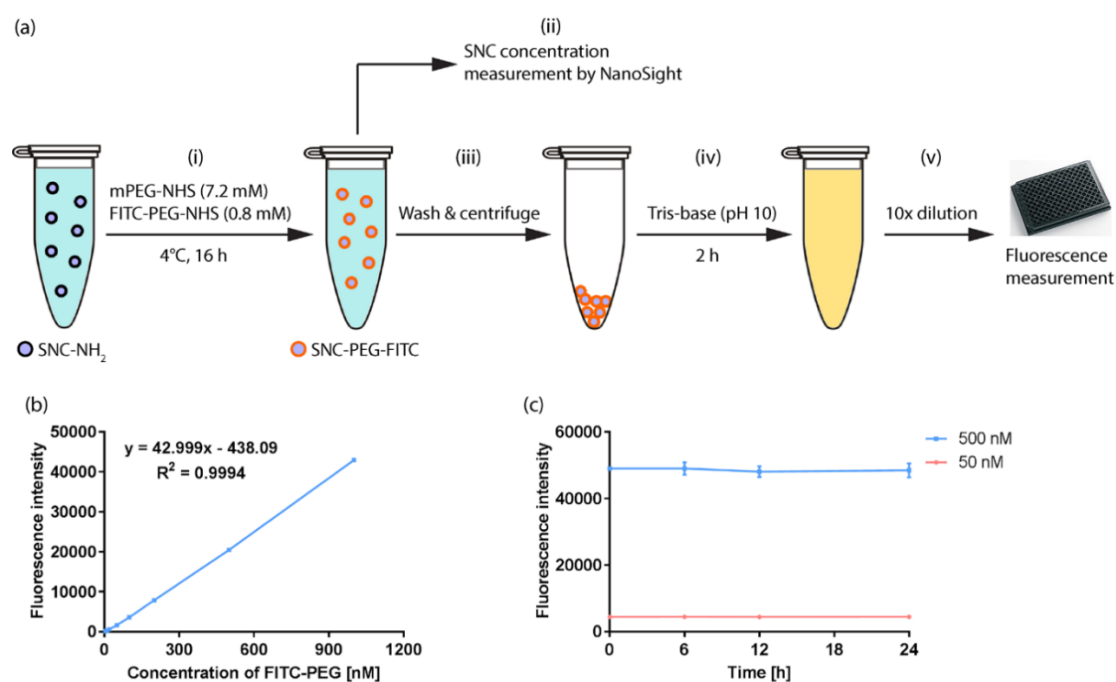


Fig. S4. (a) Experimental processes for determining the PEG density on SNC surface: i) NH_2 -functionalized SNCs were coated with PEG and FITC-PEG (10% molar percentage); ii) the concentrations of SNCs were measured using NanoSight; iii) surface modified SNCs were washed and collected, followed by iv) dissolving the SNCs using Tris-base buffer (1M, pH 10); v) the solution containing fluorescent FITC-PEG molecules was diluted by a factor of 10, with its fluorescence intensity measured. (b) Standard curve of the FITC-PEG-NHS in Tris-base buffer solution (1M, pH 10). (c) Fluorescence intensity change of 50 and 500 nM FITC-PEG-NHS at 4°C for 24 h in HEPES buffer (25 mM, pH 7.5).

Table S1. Quantification of PEG density on the surface of SNCs.^a

| Molar percentage of TEOS | 0 | 5 | 10 | 20 | 40 | 100 |
|--------------------------------------------------------------|-------|-------|-------|-------|-------|-------|
| Fluorescence intensity | 32826 | 34047 | 34482 | 36180 | 36358 | 35653 |
| FITC-PEG concentration [nM] | 773.5 | 801.9 | 812.0 | 851.5 | 855.7 | 839.3 |
| Total PEG concentration ^b [μ M] | 77.4 | 80.2 | 81.2 | 85.2 | 85.6 | 83.9 |
| SNC concentration ^c [10^{10} /mL] | 46.0 | 53.9 | 54.5 | 53.6 | 47.6 | 46.6 |
| Surface PEG density ^d [molecule/nm ²] | 0.94 | 0.83 | 0.82 | 0.88 | 0.96 | 0.89 |

^aValues are means;

^bThe overall PEG concentration is 10 times of the FITC-PEG concentration;

^cThe concentrations of SNCs were determined by nanoparticle tracking analysis using NanoSight;

^dThe surface PEG density of SNCs was calculated based on function:

$$\text{Surface PEG density} = \frac{\text{Number of PEG molecules}}{\text{Number of SNCs} \times \text{Surface area of one SNC (A)}}$$

Where the surface area of SNC (A) was calculated based on function:

$$A = \pi \cdot d^2$$

Where d is the z-averaged diameter of unmodified SNCs.

Interactions between the SNCs and cells

1). Re-arranged cellular uptake data of SNCs by RAW264.7, MCF-7 and SKOV3 cells

Our previous study compared the cellular uptake of two types of SNCs having very low (~ 700 kPa) and very high (9.7 GPa) Young's moduli for their macrophage uptake by RAW264.7 cells, and their non-specific and ligand-receptor mediated tumor cell uptake by MCF-7 and SKOV3 cells (Fig. S5a) (16). The macrophage uptake of the soft SNCs was much lower than the stiff ones for both PEG-modified and FA-PEG-modified SNCs, whereas the uptakes of PEG-modified SNCs by both SKOV3 and MCF-7 tumor cells were independent of their stiffness. But the receptor-mediated uptake of stiff FA-PEG-modified SNCs by the FR-positive SKOV3 cells was much higher than that of the soft ones, whereas they displayed similar uptake in FR-negative MCF-7 cells.

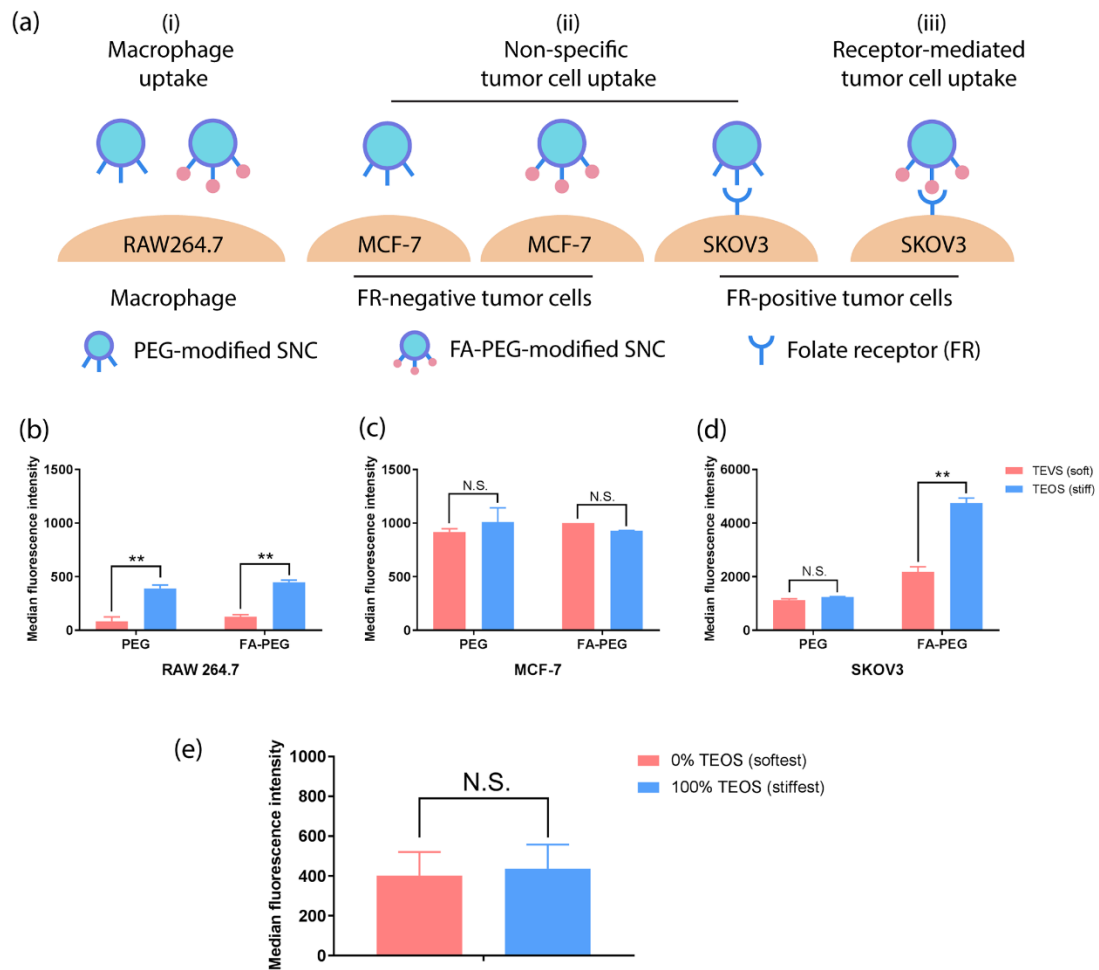


Fig. S5. Re-arranged data for the cellular uptake of PEG- and FA-PEG-modified, soft (700kPa) and stiff (9.7 GPa) SNCs by RAW264.7, MCF-7 and SKOV3 cells (16). (a) Schematic illustration showing different types of SNC–cell interactions. (b) Macrophage uptake of SNCs by RAW264.7 cells. (c) Uptake of SNCs by MCF-7 cells and (d) SKOV3 cells. (e) Cellular binding of the PEG-modified softest (0% TEOS, 560 kPa) and stiffest (100% TEOS, 1.18 GPa) SNCs to SKOV3 cells.

Morphological change of SNCs during receptor-mediated interactions with cells

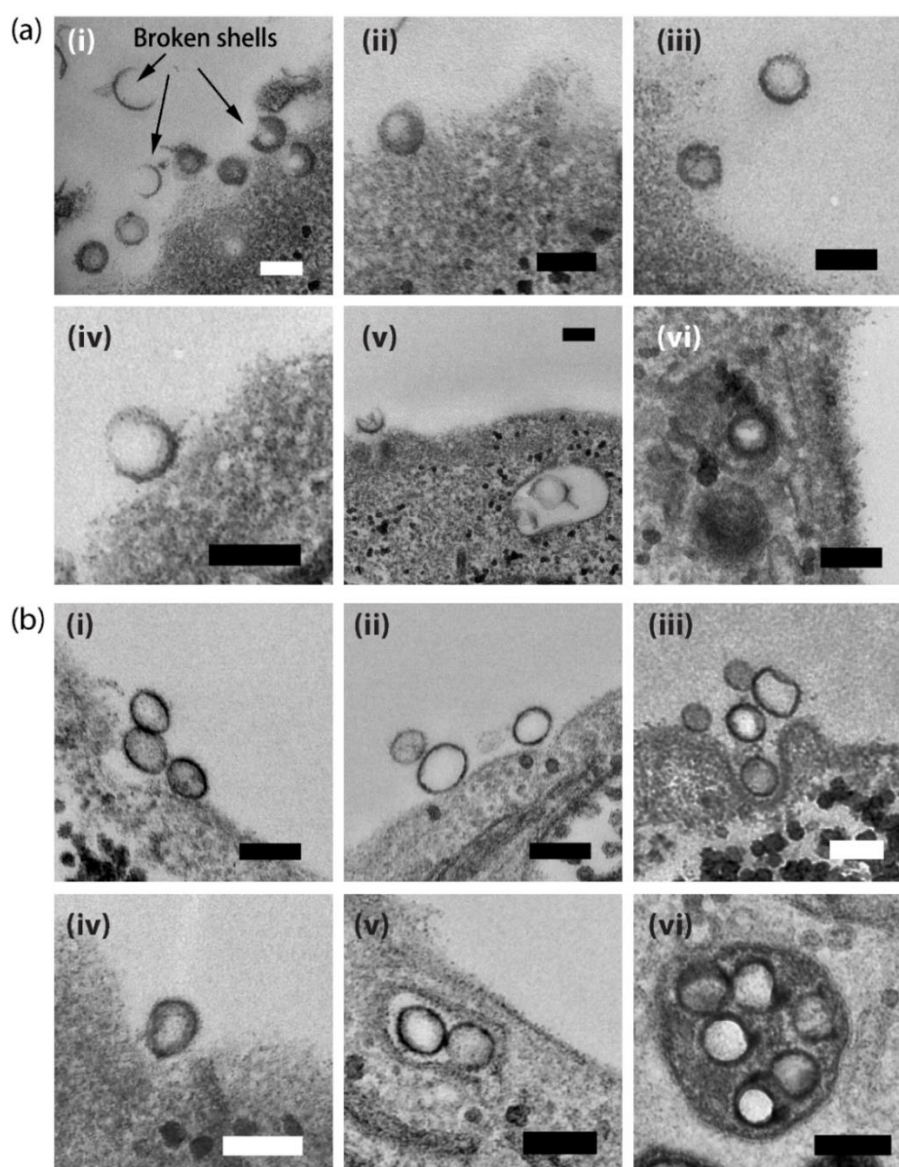
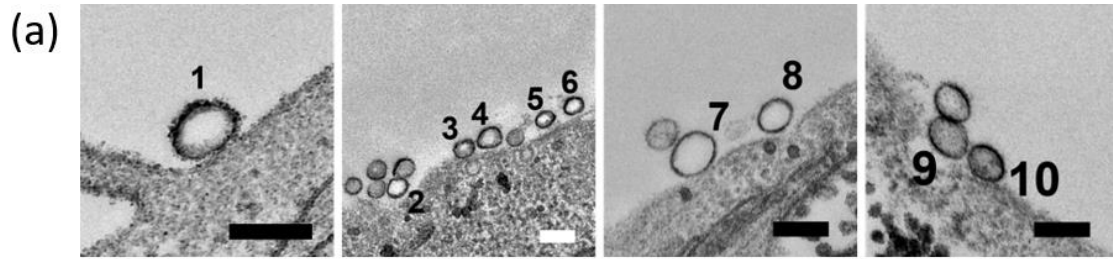
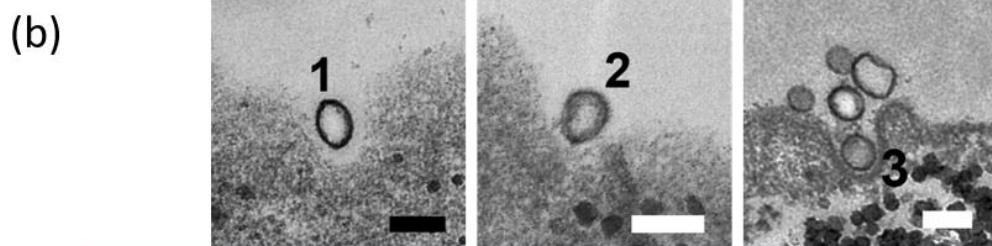


Fig. S6. TEM images showing the morphological change of FA-PEG-modified stiffest and softest SNCs during FR-mediated interactions with SKOV3 cells. (a) Stiffest SNCs (100% TEOS): (i)-(v) on cell surface; (v) and (vi) in endosome. (b) Softest SNCs (0% TEOS): (i) and (ii) on cell surface; (iii) and (iv) during internalization; (v) in endosome; (vi) in lysosome. Scale bars = 200 nm.



| Sample No. | Long axis/nm | Short axis/nm | Dimension ratio (long axis/short axis) |
|-----------------|--------------------|-------------------|-------------------------------------------|
| 1 | 159.49 | 108.08 | 1.476 |
| 2 | 126.75 | 106.16 | 1.194 |
| 3 | 113.21 | 84.24 | 1.344 |
| 4 | 150.22 | 102.97 | 1.459 |
| 5 | 115.79 | 83.35 | 1.389 |
| 6 | 113.97 | 80.42 | 1.417 |
| 7 | 180.91 | 133.42 | 1.356 |
| 8 | 132.76 | 100.03 | 1.327 |
| 9 | 145.98 | 104.14 | 1.402 |
| 10 | 122.81 | 89.35 | 1.374 |
| Ave. \pm S.D. | 136.19 \pm 22.49 | 99.22 \pm 15.85 | 1.374 \pm 0.08 |



| Sample No. | Long axis/nm | Short axis/nm | Dimension ratio (long axis/short axis) |
|-----------------|--------------------|-------------------|-------------------------------------------|
| 1 | 184.06 | 127.5 | 1.444 |
| 2 | 153.74 | 126.05 | 1.220 |
| 3 | 153.9 | 133.21 | 1.155 |
| Ave. \pm S.D. | 163.90 \pm 17.46 | 128.92 \pm 3.79 | 1.273 \pm 0.15 |

Fig. S7. Axis dimension ratio of the softest SNCs during (a) cellular binding and (b) internalization. Data are measured using NanoMeasurer software (v. 1.2.0).

Morphological change of SNCs during macrophage uptake and non-specific cancer cell uptake

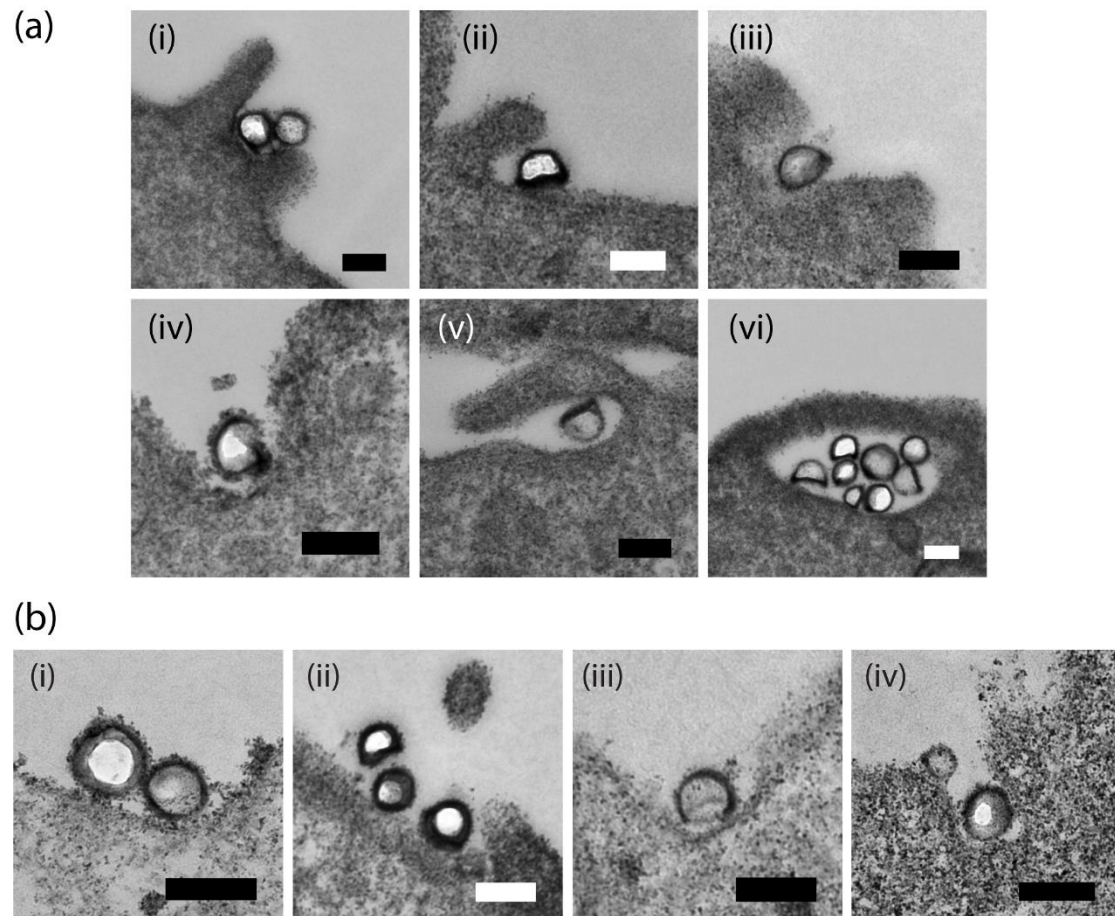


Fig. S8. TEM images showing the morphological change of the FA-PEG-modified softest SNCs (0% TEOS) (a) during macrophage uptake by RAW264.7 cells. (i)-(v) during internalization; (vi) after being internalized (in phagosome); and (b) during non-specific interaction with SKOV3 cells. (i) and (ii) on cell surface; (iii) and (iv) during internalization.

Theoretical calculation demonstrating the ability of cells to deform the softest SNCs in cellular uptake

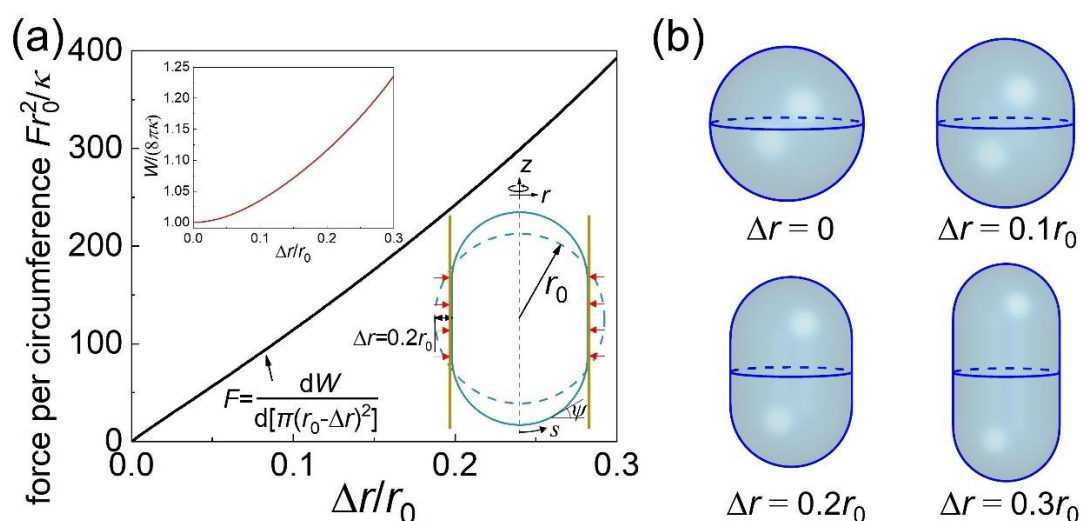


Fig. S9. Soft nanocapsule upon radial compression induced by inward pushing force (red arrows) exerted by the actin network underneath the cell membrane.

The deformed soft nanocapsule in cellular uptake is modelled as a hollow elastic capsule with a thin elastic shell confined in a rigid cylindrical tube undergoing radial shrinking. (a) The normalized force per contact circumference $F = dW/d[\pi(r_0 - \Delta r)^2]$ as a function of the normalized radius change $\Delta r / r_0$ of the shrinking cylindrical tube. Insets: total free energy W as a function of $\Delta r / r_0$ (upper left); equilibrium nanocapsule shapes at $\Delta r = 0$ (dashed line) and $0.2 r_0$ (solid line) (lower right). (b) Selected equilibrium configurations of deformed nanocapsules at different values of $\Delta r / r_0$.

Fig. 3d in the main text and Fig. S9 demonstrate that soft nanocapsules adopt a shape of prolate spheroid in the middle stage of the clathrin-mediated endocytosis and phagocytosis. Here we propose a minimal biophysical model to analyze the mechanical behavior of the wrapped nanocapsule upon the inward pushing force from actin polymerization in a ring surrounding the wrapped region. In the case of soft

nanocapsules, the actin network around the wrapped region is modelled as a rigid cylindrical wall with the capsule confined therein. The bending energy of the thin elastic shell of the wrapped capsule is modeled using the Helfrich energy as $W=2\kappa \int H^2 dA$ (34), where κ , H , and dA are the bending rigidity, mean curvature, and area element of the capsule shell, respectively. In the axisymmetric configuration of our interest, we have $H=(d\psi/ds+\sin\psi/r)/2$ with ψ , r , and s as the tangent angle, r -coordinate, and arclength of the capsule profile, respectively. The arclength s originates from the south pole of the capsule (Fig. S9a). The surface area of the capsule is fixed at $A=4\pi r_0^2$. Introducing the tangent angle ψ of the capsule profile, the bending energy W can be expressed as a function of ψ with the help of geometric relations $dr/ds=\cos\psi$ and $dz/ds=\sin\psi$. Using a representation based on the cubic B-spline function, ψ can be approximated in a form as $\psi(s)=\sum a_i N_i(s)$ ($i=0,\dots,n$), where the control points a_i as the coefficients of the basic functions $N_i(s)$ are determined numerically using the interior-point method in constrained nonlinear numerical optimization to minimize the bending energy W of the deformed capsule (42). An inequality constraint on the maximum of the r -coordinate of the capsule profile ($r\leq r_0-\Delta r$) is employed to prevent the penetration of the capsule by the shrinking cylinder. At a given $\Delta r/r_0$, the tangent angle ψ and corresponding capsule configuration associated with the minimum energy state can be determined. Then the force per contact circumference $F=dW/d[\pi(r_0-\Delta r)^2]$ is obtained numerically.

Fig. S9 indicates that the force F and bending energy W increase as Δr increases, where Δr represents the radius change of the shrinking cylindrical tube. The shapes of selected nanocapsules at different values of $\Delta r/r_0$ are given in Fig. S9b.

Fig. S9 shows that the capsule radius r_0 is around 100 nm and the shell thickness h is around 10 nm, from which we know that the capsules can be described as thin shells

($h/r_0 \ll 1$). Based on the indentation analysis, we can determine the Young's modulus E_s of the capsule shell (E_s here is the Young's modulus of the nanocapsule shell material, instead of the effective Young's modulus of the nanocapsule reported in the manuscript) using the Reissner theory (43) for thin-shelled capsules as

$$E_s = \frac{r_0 \sqrt{3(1-\nu^2)} F}{4h^2 \delta},$$

where F is the indentation force, δ is the indentation depth, and ν is the Poisson ratio of the shell. For the softest silica nanocapsule (0% TEOS) with $h/r_0=0.1$ and $\nu=0.3$ as taken, we have $E_s=1.59 \times 10^7$ N/m² by fitting the equation above with the F - δ curve in Fig. S3b. The effective bending stiffness of the capsule shell is given by

$$\kappa = \frac{E_s h^3}{12(1-\nu^2)},$$

and we have $\kappa \approx 350 k_B T$ for the softest nanocapsule.

The polymerization of a single actin filament can generate pushing force $f \approx 1.5$ pN (44). The diameter D of the area to which the active pushing force associated with a single actin filament is applied falls in a range of 2 nm~7 nm (45). The average intensity of pushing force exerted by actin filaments $f/(\pi D^2/4)$ could be in a range of 3.9×10^4 N/m² to 4.77×10^5 N/m².

Theoretical results in Fig. S9 indicate that $F r_0^2 / \kappa \approx 250$ at $\Delta r / r_0 = 0.2$. Taking $\kappa = 350 k_B T$ for the softest nanocapsule, $r_0 = 100$ nm, and assuming the height of the contact region is comparable to r_0 , we can determine the pushing force intensity as $F/r_0 = 3.6 \times 10^5$ N/m², falling in the range of $f/(\pi D^2/4)$ estimated above. In other words, the cells are able to generate the pushing forces necessary for the softest nanocapsule deformation.

REFERENCES AND NOTES

1. P. G. Gillespie, R. G. Walker, Molecular basis of mechanosensory transduction. *Nature* **413**, 194–202 (2001).
2. T. Luo, K. Mohan, P. A. Iglesias, D. N. Robinson, Molecular mechanisms of cellular mechanosensing. *Nat. Mater.* **12**, 1064–1071 (2013).
3. Y. Qiu, A. C. Brown, D. R. Myers, Y. Sakurai, R. G. Mannino, R. Tran, B. Ahn, E. T. Hardy, M. F. Kee, S. Kumar, G. Bao, T. H. Barker, W. A. Lam, Platelet mechanosensing of substrate stiffness during clot formation mediates adhesion, spreading, and activation. *Proc. Natl. Acad. Sci. U.S.A.* **111**, 14430–14435 (2014).
4. V. Vogel, M. Sheetz, Local force and geometry sensing regulate cell functions. *Nat. Rev. Mol. Cell Biol.* **7**, 265–275 (2006).
5. D. E. Discher, P. Janmey, Y.-L. Wang, Tissue cells feel and respond to the stiffness of their substrate. *Science* **310**, 1139–1143 (2005).
6. A. S. Yap, K. Duszyc, V. Viasnoff, Mechanosensing and mechanotransduction at cell–cell junctions. *Cold Spring Harb. Perspect. Biol.* **10**, a028761 (2017).
7. M. Morimatsu, A. H. Mekhdjian, A. S. Adhikari, A. R. Dunn, Molecular tension sensors report forces generated by single integrin molecules in living cells. *Nano Lett.* **13**, 3985–3989 (2013).
8. X. Wang, T. Ha, Defining single molecular forces required to activate integrin and notch signaling. *Science* **340**, 991–994 (2013).
9. X. Banquy, F. Suarez, A. Argaw, J.-M. Rabanel, P. Grutter, J.-F. Bouchard, P. Hildgen, S. Giasson, Effect of mechanical properties of hydrogel nanoparticles on macrophage cell uptake. *Soft Matter* **5**, 3984–3991 (2009).

10. J. Sun, L. Zhang, J. Wang, Q. Feng, D. Liu, Q. Yin, D. Xu, Y. Wei, B. Ding, X. Shi, X. Jiang, Tunable rigidity of (polymeric core)–(lipid shell) nanoparticles for regulated cellular uptake. *Adv. Mater.* **27**, 1402–1407 (2015).
11. A. C. Anselmo, M. Zhang, S. Kumar, D. R. Vogus, S. Menegatti, M. E. Helgeson, S. Mitragotri, Elasticity of nanoparticles influences their blood circulation, phagocytosis, endocytosis, and targeting. *ACS Nano* **9**, 3169–3177 (2015).
12. A. C. Anselmo, S. Mitragotri, Impact of particle elasticity on particle-based drug delivery systems. *Adv. Drug Deliv. Rev.* **108**, 51–67 (2017).
13. Z. Teng, C. Wang, Y. Tang, W. Li, L. Bao, X. Zhang, X. Su, F. Zhang, J. Zhang, S. Wang, D. Zhao, G. Lu, Deformable hollow periodic mesoporous organosilica nanocapsules for significantly improved cellular uptake. *J. Am. Chem. Soc.* **140**, 1385–1393 (2018).
14. P. Guo, D. Liu, K. Subramanyam, B. Wang, J. Yang, J. Huang, D. T. Auguste, M. A. Moses, Nanoparticle elasticity directs tumor uptake. *Nat. Commun.* **9**, 130 (2018).
15. M. Yu, L. Xu, F. Tian, Q. Su, N. Zheng, Y. Yang, J. Wang, A. Wang, C. Zhu, S. Guo, X. Zhang, Y. Gan, X. Shi, H. Gao, Rapid transport of deformation-tuned nanoparticles across biological hydrogels and cellular barriers. *Nat. Commun.* **9**, 2607 (2018).
16. Y. Hui, D. Wibowo, Y. Liu, R. Ran, H.-F. Wang, A. Seth, A. P. J. Middelberg, C.-X. Zhao, Understanding the effects of nanocapsular mechanical property on passive and active tumor targeting. *ACS Nano* **12**, 2846–2857 (2018).
17. Y. Chen, L. Ju, M. Rushdi, C. Ge, C. Zhu, V. M. Weaver, Receptor-mediated cell mechanosensing. *Mol. Biol. Cell* **28**, 3134–3155 (2017).
18. D. Wibowo, C.-X. Zhao, A. P. J. Middelberg, Emulsion-templated silica nanocapsules formed using bio-inspired silicification. *Chem. Commun.* **50**, 11325–11328 (2014).
19. L. Adumeau, C. Genevois, L. Roudier, C. Schatz, F. Couillaud, S. Mornet, Impact of surface grafting density of PEG macromolecules on dually fluorescent silica nanoparticles used for

- the in vivo imaging of subcutaneous tumors. *Biochim. Biophys. Acta. Gen. Subj.* **1861**, 1587–1596 (2017).
20. A. Lesniak, A. Salvati, M. J. Santos-Martinez, M. W. Radomski, K. A. Dawson, C. Åberg, Nanoparticle adhesion to the cell membrane and its effect on nanoparticle uptake efficiency. *J. Am. Chem. Soc.* **135**, 1438–1444 (2013).
 21. X. Yi, X. Shi, H. Gao, Cellular uptake of elastic nanoparticles. *Phys. Rev. Lett.* **107**, 098101 (2011).
 22. X. Yi, H. Gao, Kinetics of receptor-mediated endocytosis of elastic nanoparticles. *Nanoscale* **9**, 454–463 (2017).
 23. Z. Shen, H. Ye, X. Yi, Y. Li, Membrane wrapping efficiency of elastic nanoparticles during endocytosis: Size and shape matter. *ACS Nano* **13**, 215–228 (2019).
 24. J. A. Champion, S. Mitragotri, Role of target geometry in phagocytosis. *Proc. Natl. Acad. Sci. U.S.A.* **103**, 4930–4934 (2006).
 25. J. Gilden, M. F. Krummel, Control of cortical rigidity by the cytoskeleton: Emerging roles for septins. *Cytoskeleton* **67**, 477–486 (2010).
 26. G. T. Charras, J. C. Yarrow, M. A. Horton, L. Mahadevan, T. J. Mitchison, Non-equilibration of hydrostatic pressure in blebbing cells. *Nature* **435**, 365–369 (2005).
 27. R. Pablo, M. Veronika, C. Dianne, Generation of membrane structures during phagocytosis and chemotaxis of macrophages: Role and regulation of the actin cytoskeleton. *Immunol. Rev.* **256**, 222–239 (2013).
 28. M. Saleem, S. Morlot, A. Hohendahl, J. Manzi, M. Lenz, A. Roux, A balance between membrane elasticity and polymerization energy sets the shape of spherical clathrin coats. *Nat. Commun.* **6**, 6249 (2015).

29. S. Boulant, C. Kural, J.-C. Zeeh, F. Ubelmann, T. Kirchhausen, Actin dynamics counteract membrane tension during clathrin-mediated endocytosis. *Nat. Cell Biol.* **13**, 1124–1131 (2011).
30. D. K. Cureton, R. H. Massol, S. Saffarian, T. L. Kirchhausen, S. P. J. Whelan, Vesicular stomatitis virus enters cells through vesicles incompletely coated with clathrin that depend upon actin for internalization. *PLOS Pathog.* **5**, e1000394 (2009).
31. J.-Y. Tinevez, N. Perry, J. Schindelin, G. M. Hoopes, G. D. Reynolds, E. Laplantine, S. Y. Bednarek, S. L. Shorte, K. W. Eliceiri, TrackMate: An open and extensible platform for single-particle tracking. *Methods* **115**, 80–90 (2017).
32. N. Ruthardt, D. C. Lamb, C. Bräuchle, Single-particle tracking as a quantitative microscopy-based approach to unravel cell entry mechanisms of viruses and pharmaceutical nanoparticles. *Mol. Ther.* **19**, 1199–1211 (2011).
33. Z. Shen, H. Ye, Y. Li, Understanding receptor-mediated endocytosis of elastic nanoparticles through coarse grained molecular dynamic simulation. *Phys. Chem. Chem. Phys.* **20**, 16372–16385 (2018).
34. W. Helfrich, Elastic properties of lipid bilayers: Theory and possible experiments. *Z. Naturforsch. C* **28**, 693–703 (1973).
35. J. Liu, M. Kaksonen, D. G. Drubin, G. Oster, Endocytic vesicle scission by lipid phase boundary forces. *Proc. Natl. Acad. Sci. U.S.A.* **103**, 10277–10282 (2006).
36. N. Walani, J. Torres, A. Agrawal, Endocytic proteins drive vesicle growth via instability in high membrane tension environment. *Proc. Natl. Acad. Sci. U.S.A.* **112**, E1423–E1432 (2015).
37. T. Zhang, R. Sknepnek, M. J. Bowick, J. M. Schwarz, On the modeling of endocytosis in yeast. *Biophys. J.* **108**, 508–519 (2015).

38. J. E. Hassinger, G. Oster, D. G. Drubin, P. Rangamani, Design principles for robust vesiculation in clathrin-mediated endocytosis. *Proc. Natl. Acad. Sci. U.S.A.* **114**, E1118–E1127 (2017).
39. M. Herant, V. Heinrich, M. Dembo, Mechanics of neutrophil phagocytosis: Behavior of the cortical tension. *J. Cell Sci.* **118**, 1789–1797 (2005).
40. M. Herant, V. Heinrich, M. Dembo, Mechanics of neutrophil phagocytosis: Experiments and quantitative models. *J. Cell Sci.* **119**, 1903–1913 (2006).
41. X. Huang, J. Chisholm, J. Zhuang, Y. Xiao, G. Duncan, X. Chen, J. S. Suk, J. Hanes, Protein nanocages that penetrate airway mucus and tumor tissue. *Proc. Natl. Acad. Sci. U.S.A.* **114**, E6595–E6602 (2017).
42. X. Yi, H. Gao, Cell membrane wrapping of a spherical thin elastic shell. *Soft Matter* **11**, 1107–1115 (2015).
43. E. Reissner, Stresses and small displacements of shallow spherical shells, II. *J. Math. Phys.* **25**, 279–300 (1946).
44. M. J. Footer, J. W. J. Kerssemakers, J. A. Theriot, M. Dogterom, Direct measurement of force generation by actin filament polymerization using an optical trap. *Proc. Natl. Acad. Sci. U.S.A.* **104**, 2181–2186 (2007).
45. B. Alberts, A. Johnson, J. Lewis, M. Raff, K. Roberts, P. Walter, *Molecular Biology of the Cell* (Garland Science, ed. 5, 2007).